Propagation of soil moisture memory to streamflow and evapotranspiration in Europe

Rene Orth[1] and Sonia I. Seneviratne[1]

DRAFT MANUSCRIPT

19 June 2013

[1]Institute for Atmospheric and Climate Science, ETH Zurich, Universitätstrasse 16, CH-8092 Zurich, Switzerland (rene.orth@env.ethz.ch, sonia.seneviratne@env.ethz.ch)

Abstract

As a key variable of the land-climate system soil moisture is a main driver of streamflow and evapotranspiration under certain conditions. Soil moisture furthermore exhibits outstanding memory (persistence) characteristics. Also for streamflow many studies report distinct low frequency variations that represent a memory. Using data from over 100 near-natural catchments located across Europe we investigate in this study the connection between soil moisture memory and the respective memory of streamflow and evapotranspiration on different time scales. For this purpose we use a simple water balance model in which dependencies of runoff (normalized by precipitation) and evapotranspiration (normalized by radiation) on soil moisture are fitted using streamflow observations. The model therefore allows us to compute memory of soil moisture, streamflow and evapotranspiration on the catchment scale. We find considerable memory in soil moisture and streamflow in many parts of the continent, and evapotranspiration also displays some memory at monthly time scale in some catchments. We show that the memory of streamflow and evapotranspiration jointly depend on soil moisture memory and on the strength of the coupling of streamflow and evapotranspiration to soil moisture. Furthermore we find that the coupling strengths of streamflow and evapotranspiration to soil moisture depend on the shape of the fitted dependencies and on the variance of the meteorological forcing. To better interpret the magnitude of the respective memories across Europe we finally provide a new perspective on hydrological memory by relating it to the mean duration required to recover from anomalies exceeding a certain threshold.

1 Introduction

Many past and recent publications have pointed out the remarkable persistence characteristics of soil moisture (*Delworth and Manabe* 1988, *Vinnikov and Yeserkepova* 1990, *Entin et al.* 2000, *Koster and Suarez* 2001, *Schlosser and Milly* 2002, *Wu and Dickinson* 2004, *Seneviratne et al.* 2006, *Koster et al.* 2010, *Seneviratne and Koster* 2012). This soil moisture persistence, hereafter referred to as "memory", is caused by the integrative nature of soil moisture as water storage. It has been found in observations and models, at point scale and on continental scales. Furthermore also for other land-surface variables, persistence characteristics have been reported, even if less pronounced than for soil moisture. For instance streamflow exhibits distinct low frequency variations that represent a memory resulting from a recession behavior of the streamflow response following a precipitation event (*Rodriguez-Iturbe and Valdes* 1979, *Lins* 1997, *Labat* 2008, *Gudmundsson et al.* 2011).

Given the important role of soil moisture in the hydrological system and for land-atmosphere interactions (e.g. *Seneviratne et al.* 2010 for a review), the question arises if its memory may propagate to other quantities that are at least partly driven by soil moisture. For example, runoff and evapotranspiration may be highly dependent on soil moisture under certain conditions (*Eagleson* 1978, *Koster and Milly* 1997, *Koster et al.* 2004, *Botter et al.* 2007, *Bisselink and Dolman* 2009, *Kirchner* 2009, *Teuling et al.* 2009), therefore soil moisture memory may induce persistence in these quantities.

This study investigates under which conditions and to which extent soil moisture memory may propagate to streamflow and/or evapotranspiration. In case of streamflow, this question is of high importance in relation with flood prediction and water resource management. An evapotranspiration memory has implications on the exchange of water between the land and the atmosphere, as well as on near-surface temperature because evapotranspiration is (negatively) related with sensible heat flux. Following the approach proposed in *Orth et al.* (2013), we calibrate a simple hydrological model (*Koster and Mahanama* 2012) with streamflow measurements from 100 catchments across Europe to infer memory characteristics of soil moisture, streamflow and evapotranspiration. We identify drivers and properties of the memory propagation and investigate their dependencies on regional features. Moreover we determine favorable climate and land-atmosphere regimes that promote memory propagation into the climate system. In the last part of this study we investigate how the memories in soil moisture, streamflow and evapotranspiration change under dry and wet conditions, which is especially relevant in the context of the predictability of extreme events (*Koster et al.* 2010, *Mueller and Seneviratne* 2012).

2 Methodology

2.1 Simple water-balance model

We use a simple water-balance model adapted from *Koster and Mahanama* (2012) in this study. The revised formulation used here has been introduced and discussed in *Orth et al.* (2013). As in that study, we run the model with a daily time step. The model is based on the following water-balance equation:

$$w_{n+\triangle t} = w_n + (P_n - E_n - Q_n)\,\triangle t \tag{1}$$

where w_n, the only prognostic variable of the model (in mm), is the total soil moisture content at the beginning of time step n. Between time step n and $n + \triangle t$, the soil moisture content is changed by the accumulated precipitation P_n, evapotranspiration E_n, and runoff Q_n (all in $\frac{mm}{d}$), to yield an updated soil moisture content $w_{n+\triangle t}$ at the beginning of the following time step. Note that the employed simple model is highly conceptual, and that w_n by definition stands for the total soil moisture content. As in *Orth et al.* 2013, we run the model in this study with a time step of one day ($\triangle t = 1d$).

2.1.1 Runoff and evapotranspiration dependencies on soil moisture

In the simple water-balance model, evapotranspiration (normalized by net radiation) depends on soil moisture (scaled with the water holding capacity) only:

$$\frac{\lambda \rho_w E_n}{R_n} = \beta_0 \left(\frac{w_n}{c_s}\right)^{\gamma} \; with\; \gamma > 0 \; and \; \beta_0 \leq 1 \tag{2}$$

where R_n denotes net radiation (in $\frac{W}{m^2}$), λ is the latent heat of vaporization (in $\frac{J}{kg}$), ρ_w is the density of water (in $\frac{kg}{m^3}$) and c_s is a model parameter that refers to the water holding capacity of the soil (in mm). Another model parameter, β_0 (unitless), allows to capture the evaporative resistance of the soil and the vegetation, whereas the parameter γ (also unitless) ensures a strictly monotonically increasing evapotranspiration ratio $\frac{\lambda \rho_w E_n}{R_n}$

Similarly to evapotranspiration (ET), runoff normalized by precipitation depends on soil moisture only:

$$\frac{Q_n}{P_n} = \left(\frac{w_n}{c_s}\right)^{\alpha} \; with \; \alpha \geq 0 \tag{3}$$

where the exponent α ensures an increasing runoff ratio $\frac{Q_n}{P_n}$ with increasing soil moisture.

In order to account for the transport of subsurface runoff to streambeds and the traveling time of surface runoff to the stream gauge site, *Orth et al.* (2013) distinguish between runoff and streamflow. The latter is computed from the simulated runoff with an imposed delay:

$$S_{n+t} = Q_n \frac{1}{\tau} e^{-\frac{t}{\tau}} \tag{4}$$

where τ refers to the delay time scale (in $days$) that determines the streamflow S_{n+t} at time $n+t$ which results from the runoff Q_n at time n. The integral of $\frac{1}{\tau} e^{-\frac{t}{\tau}}$ equals 1 as $t \rightarrow \infty$, such that all runoff is converted to streamflow. The total streamflow at any time step can be computed from the previously generated runoff amounts:

$$S_n = \sum_{i=0}^{60} Q_{n-i\triangle t} \left(e^{-\frac{i\triangle t}{\tau}} - e^{-\frac{(i+1)\triangle t}{\tau}} \right) \tag{5}$$

As in *Orth et al.* (2013) we compute the streamflow from the runoff amounts generated during the 60 preceding time steps to account for > 99 of the runoff water.

To investigate the connection between streamflow and precipitation we furthermore define here the cumulative weighted precipitation, which is the precipitation used to compute the runoff amounts that contribute to streamflow at time n:

$$P_n^* = \sum_{i=0}^{60} P_{n-i\triangle t} \left(e^{-\frac{i\triangle t}{\tau}} - e^{-\frac{(i+1)\triangle t}{\tau}} \right) \tag{6}$$

.

2.1.2 Parameter fitting

In total 5 model parameters ($c_s, \alpha, \tau, \beta_0, \gamma$) have to be fitted to determine runoff, evapotranspiration and streamflow of a catchment. This is done for each catchment using the same optimization approach as *Orth et al.* (2013), whereby the optimal set of parameters is determined as the set that yields the best fit between modeled and observed streamflow among 25 estimated sets (representing local maxima in the five-dimensional parameter space). This fit is evaluated as a correlation during July, August and September of all available years to avoid an impact of snow, which is not included in the model. As in *Orth et al.* (2013), we use a correlation to determine the fit because our focus is on the simulation of the temporal evolution of soil moisture and streamflow rather than on their absolute amount, because this is important to represent memory characteristics. Table 1 summarizes the accuracies with which the parameters are fitted (i.e. the step width for each parameter as applied in the optimization procedure), their upper and lower limits as well as maxima and minima of the actual parameter values found for the catchments considered in this study (see Section 3). Note that in contrast to *Orth et al.* (2013), we apply here upper limits to the exponents α and γ (15) and the water holding capacity c_s (2000 mm) to accelerate the optimization process and to prevent unreasonable fitted parameter values.

2.2 Computation of slopes

To quantify the impact of soil moisture on streamflow and ET, we use the slopes of the runoff and ET functions (Equations (5) and (2)) normalized with precipitation and net radiation, respectively. These slopes are catchment-specific and depend only on the soil moisture content and on the fitted parameters. They are computed as follows: For every daily soil moisture value that occurs between May and September over the whole considered time period (see Section 3) in a particular catchment we compute the respective slopes of the normalized runoff and ET functions from their derivations with respect to soil moisture. Then we take the mean of all the slopes to derive a mean runoff function slope and a mean ET function slope for a particular catchment.

As described and illustrated later in Section 4.2 the runoff and ET function slopes are important variables for the soil moisture-streamflow and soil moisture-ET coupling strength, such that for instance a slope of zero implies no impact of soil moisture, whereas a high slope tends to translate soil moisture changes into changes of streamflow or ET.

2.3 Computation of memory

To determine the persistence of soil moisture, streamflow and ET that are produced by the simple water-balance model, we calculate the respective memory as an inter-annual correlation over a particular lag (see *Koster and Suarez* 2001 and *Seneviratne and Koster* 2012): For a given quantity, the estimates of day n from all years are correlated with the estimates of day $n + t_{lag}$ from all years. To derive representative memory estimates for half-monthly periods, we compute inter-annual correlations for this period and for the preceding and subsequent 30 days (as introduced by *Orth and Seneviratne* 2012 and also applied by *Orth et al.* 2013). For soil moisture memory, this corresponds to the following expression:

$$\rho\left(w_n, w_{n+t_{lag}}\right) = \frac{1}{t_{end} - t_{start} + 60 - t_{lag}} \sum_{i=t_{start}-30}^{t_{end}+30-t_{lag}} \rho\left(w_i, w_{i+t_{lag}}\right) \tag{7}$$

where t_{start} and t_{end} refer to the respective start and end dates of the considered half-monthly time period. Starting 30 days prior to the beginning of the half-monthly interval and finishing $30 - t_{lag}$ days after the end of the half-monthly period, we obtain a number of correlations of which we take a trimmed average (not shown in Equation (7); we avoid the 10% highest and 10% lowest values, as in *Orth et al.* 2013) to yield a representative memory estimate for the particular half-monthly period.

In order to study the connection between soil moisture memory and the memory of streamflow and ET, respectively, we consider in the following 30-day-lag memories that are computed as described above for all quantities. To assess the impact of the investigated time scale we perform the same analysis using monthly averaged data from which we compute the respective 1-month-lag memories.

2.4 Computation of persistence time scales

While memory is considered as lag correlation in the previous subsection and previous studies (e.g. *Koster and Suarez* 2001, *Orth and Seneviratne* 2012), we relate the memories of soil moisture, streamflow and ET in this study also to persistence time scales. This is more easily interpretable and allows us to study the respective memories under different hydrological conditions.

For the computation of this persistence time scale we proceed as follows: (i) We define "normal" conditions at a particular day as those differing at most by one standard deviation (computed over the values of that day from all years) from the mean of that day over all years; (ii) We choose deviations of 1.33 and 1.66 standard deviations from the mean as thresholds for medium and strong anomalies, respectively; (iii) We select all days of the time

series between May and September (focusing on the warm season we avoid cold season impacts due to snow and land cover change) that exceed a threshold and calculate for each day the delay until which the quantity of interest recovers to normal conditions; (iv) Finally, we take the mean of all the durations to derive a mean persistence of anomalous conditions once they have exceeded a certain threshold.

Comparing the persistence time scale to respective memories expressed as lag correlations, we can relate these correlations to mean recovery times from respective anomalies determined by a chosen threshold.

2.5 Coupling of streamflow and evapotranspiration to soil moisture

As this study is investigating the propagation of memory from soil moisture to streamflow and ET, it is necessary to assess the extent to which streamflow and ET are driven by soil moisture. For this purpose, we introduce a measure of the coupling strength between soil moisture and streamflow, or soil moisture and ET, respectively. We define the coupling strength between soil moisture and streamflow (hereafter referred to as soil moisture-streamflow coupling strength) as the correlation between them, $\rho\left(S_n, w_n\right)$. Similarly, to measure the coupling strength between soil moisture and ET (hereafter referred to as soil moisture-ET coupling strength), we use $\rho\left(E_n, w_n\right)$.

The computation of these correlations is performed in a similar way as in Equation (7). Instead of correlating estimates of a given quantity at day n from all years with the estimates of day $n + t_{lag}$ from all years, we correlate estimates of one quantity at day n from all years with estimates of the other quantity at the same day n of all years. Similar to memory, the coupling strengths are also computed as representative estimates for half-monthly periods.

Using these estimates we can determine and compare the respective coupling strengths with each other, in different seasons, and across the various catchments (see Section 3).

3 Data

In order to derive a spatially distributed evaluation of soil moisture, streamflow and ET memory across Europe we apply the simple water-balance model to near-natural catchments (i.e. catchments with negligible human impact) located throughout Europe. The corresponding streamflow data stem from a dataset compiled by *Stahl et al.*

(2010), who collected data from the European water archive (http://grdc.bafg.de [checked on 16 July 2012]), from national ministries and meteorological agencies, as well as from the WATCH project (http://www.eu-watch.org [checked on 16 July 2012]).

The simple model uses precipitation and radiation information as an input. We use satellite-measured net radiation from the NASA/GEWEX SRB project (http://eosweb.larc.nasa.gov/PRODOCS/srb/table_srb.html [checked on 16 July 2012]). The precipitation data was obtained from the E-OBS dataset (http://eca.knmi.nl [checked on 16 July 2012]), which is an interpolation of rain gauge measurements on a regular grid across Europe, and which was developed by the ENSEMBLES project (http://ensembles-eu.metoffice.com [checked on 16 July 2012]).

Note that this study therefore uses only observed (streamflow, net radiation) or observationally-based (precipitation) data. Given the different limitations in data availability of streamflow, precipitation and radiation, we consider a time period of 17 years between 1984 and 2000.

3.1 Selection of catchments

Given the large number of >400 catchments contained in the *Stahl et al.* (2010) dataset, we had to select a subset for two reasons: (i) the parameter fitting procedure (Section 2.1.2) is computationally demanding and (ii) in a few catchments the fitting procedure did not work well as seen from a low correlation between modeled and observed streamflow, probably due to impacts of snow (which is not included in the model).

Running the parameter fitting procedure with 5 instead of 25 iterations (see Section 2.1.2) for all catchments to reduce the computational effort (thereby increasing the risk that the resulting parameter set is only a local instead of a global maximum in the five-dimensional parameter space), we selected 100 catchments for this study, for which the streamflow optimization (see Section 2.1.2) yielded the highest correlations. For the selected 100 catchments we then performed the parameter fitting procedure another 20 times to ensure that we find the global optimum of the parameters. Corresponding information on name, coordinates, river, size, altitude and mean streamflow of the considered catchments is provided in Appendix A. Their locations together with their mean daily streamflow are displayed in Figure 1. The catchments are well-distributed across the continent, except for the south-east, thus allowing an analysis of persistence across a large area. As can be inferred from Table 1, the range of the fitted parameter values is larger compared to *Orth et al.* (2013) as we consider many more catchments, which are moreover distributed over a much wider area and across a broader range of climate regimes.

4 Results

In this section we first present an evaluation of the simple model's simulated streamflow and its memory in the considered catchments, followed by a case study to illustrate the model behavior under different hydrological conditions. Thereafter we investigate the connection between soil moisture memory on the one hand and streamflow and ET memory on the other hand, including an identification of the main driving mechanisms of these relationships. In the last part of this section we present a different view on memory; we quantify its strength as a recovery time from anomalous conditions, and we investigate its variations with extreme conditions.

4.1 Evaluation of modeled streamflow

The employed water-balance model was earlier validated at 13 Swiss catchments in *Orth et al.* (2013), with a focus on soil moisture memory. However, the present study also focuses on streamflow memory and considers a much wider region that covers a large fraction of Europe. Hence, we provide an evaluation of the performance of the simple water-balance model with respect to its representation of mean streamflow and streamflow memory at the investigated catchments. To allow an independent validation we consider monthly averages for June and October in all catchments as these months are not part of the optimization period in which the model is calibrated (see Section 2.1.2). The results are displayed in Figure 2. Note that we investigate here the subset of catchments described in Section 3.1 as well as the totality of the 430 catchments of the *Stahl et al.* (2010) dataset in order to show a meaningful performance of the simple water balance model also in the catchments we disregard for the remainder of this study. Note that for the excluded catchments we performed the parameter fitting procedure with 5 instead of 25 iterations (see Section 2.1.2) to reduce the computational effort (thereby increasing the risk that the resulting parameter set is only a local instead of a global maximum in the five-dimensional parameter space).

Considering all 430 catchments of the *Stahl et al.* (2010) dataset, we find a rough agreement of the modeled mean daily streamflow with observations in both months. The numerous catchments where streamflow is underestimated (especially in June) are impacted by snow melt and melting glaciers, which are both not accounted for in the model. The agreement is better when only the 100 selected catchments are considered. The fitted regression lines are closer to the identity line. The match is still slightly worse in June than in October as there are some high-altitude catchments among the selected catchments (11% of the catchments have an average altitude higher

than 1000m above sea level, see Appendix A), which may therefore be impacted by snow melt. The relatively good fit between modeled and observed mean daily streamflow is an interesting feature as only the *correlation* between modeled and observed streamflow has been used for the calibration of the model. As shown on the right hand side of Figure 2 the streamflow memory is well captured by the model for most catchments, although the regression lines indicate a slight underestimation of high memories in both months. And for the same reason discussed above the explained fraction of variance is slightly higher in October compared to June. Note that the explained fraction of variance, R^2, is higher (0.8) when comparing mean monthly memories of the selected catchments, averaged from May-September (as used in Sections 4.3 and 4.4). The agreement between modeled and observed streamflow memory is better for the selected, reduced number of catchments than for the totality of catchments, indicating that the quality of the modeled streamflow memory depends to some extent on the goodness of the streamflow optimization.

In order to further validate the simple water balance model and the parameter fitting procedure we display the fitted water holding capacities in Figure 3. The fitted values fall in a physically meaningful range. Furthermore in many regions we find similar water holding capacities for nearby catchments, underlining the robustness of the parameter fitting approach. Some few exceptions are probably due to the heterogeneous nature of soil and land cover characteristics. There are also large-scale variations; in central Germany and across France the storage capacity tends to be higher, whereas in the Alps and at the Norwegian coast we find low water holding capacities.

4.2 Case Study - Le Saulx catchment

We illustrate the model behavior and the (modeled) relationships between soil moisture, streamflow and ET under dry, average and wet conditions based on a pronounced dry-down period between April and July 1998 in the Le Saulx catchment. We chose this catchment as example because it is located in eastern France where land cover and meteorological conditions are to some extent representative for central Europe, and also because of the especially pronounced 1998 dry-down. Figure 4 shows in the upper part the runoff function (normalized by precipitation) and ET function (normalized by net radiation) fitted for that catchment based on the observed streamflow time series. As shown by the background histogram, the soil moisture content during April through October (snow-free season) generally ranges between 100 and 150 mm, where the slope of the normalized ET function is rather constant, indicating a constant sensitivity of normalized ET with respect to soil moisture. In

contrast, the slope of the normalized runoff function increases strongly over this interval and therefore also the sensitivity of normalized runoff to soil moisture varies with the soil moisture content. Under dry conditions the soil moisture content occasionally decreases to about 50 mm, which slightly increases the sensitivity of ET to soil moisture and almost prevents any runoff as the normalized runoff function is almost zero. Under wet conditions the soil moisture content may rise up to over 150 mm. Under such conditions, if the soil moisture content is still lower than the water holding capacity of 170 mm, the runoff is very strongly dependent on soil moisture, in contrast to ET that shows a decreased sensitivity under wet conditions. However, beyond soil moisture values of 170 mm all precipitation is transformed into runoff and therefore the streamflow does no longer vary with soil moisture but only with precipitation. Note that the soil moisture content may exceed the water holding capacity of 170 mm as indicated by the background histogram. This is caused by a negative net radiation forcing during winter, which induces negative ET (condensation) and therefore increasing soil moisture; in some years it takes as long as April or May to remove this moisture surplus with seasonally increasing net radiation.

Keeping these relationships in mind, the lower part of Figure 4 displays the evolution of modeled soil moisture, streamflow and ET during the April-July 1998 dry-down period together with the corresponding precipitation and net radiation forcing. The dashed red line indicating the observed streamflow evolution compares well with the modeled streamflow in terms of the temporal evolution (on which we focus, see Section 2.1.2), pointing out a reasonable performance of the model. The first month, April, is rather wet (high precipitation) and cloudy (low net radiation). Consequently, the streamflow is high, responds strongly to precipitation, and its evolution corresponds well with the soil moisture evolution, underlining the high sensitivity to soil moisture discussed above (as soil moisture is still below the water holding capacity). In contrast to streamflow, ET is lower, mostly driven by net radiation, and displays a low sensitivity to changes in soil moisture. During May and June the catchment experienced mostly sunny and dry conditions (high net radiation), only interrupted by low to medium precipitation in late May and early June. Correspondingly the soil dries out remarkably. The streamflow therefore decreases to almost zero, showing almost no response to the precipitation and the following slight increase of soil moisture. This illustrates the decoupling of streamflow from soil moisture under dry conditions. On the other hand, ET is comparatively high and roughly follows the strong soil moisture decrease and the subsequent stabilization, although net radiation is still the main driver, as a maximum in net radiation in the second half of June causes a pronounced maximum in ET (even if soil moisture is decreasing). Finally, in July soil moisture has decreased to very low levels such that the ET level is also lower and, more importantly, despite strong day-to-day variations in net radiation,

the ET evolution corresponds roughly to soil moisture.

4.3 Propagation of soil moisture memory

In contrast to the previous subsections that focused on particular months, all quantities discussed in this subsection (memories, coupling strengths, variances) are computed as a mean of all months between May and September. However, all mechanisms identified in the following also play a role for seasonal cycles of the memories of (modeled) soil moisture, streamflow and ET in the specific catchments.

4.3.1 Memory of soil moisture, streamflow and evapotranspiration

Figure 5 displays the 30-day-lag memories of soil moisture ($\rho\left(w_n, w_{n+30}\right)$), streamflow ($\rho\left(S_n, S_{n+30}\right)$) and ET ($\rho\left(E_n, E_{n+30}\right)$) computed from daily data in all catchments as compared to the respective 1-month-lag memories computed from monthly averaged data. The memory patterns derived from daily and monthly data are very similar. The 1-month-lag memories are higher, which results from the aggregation of the data that minimizes the impact of day-to-day variations in the meteorological forcing.

As reported in numerous earlier studies (e.g. *Delworth and Manabe* 1988, *Entin et al.* 2000, *Robock et al.* 2000, *Koster and Suarez* 2001, *Orth and Seneviratne* 2012) we find considerable persistence in soil moisture in almost all catchments. Largest soil moisture memory is found across Central Europe (Germany, eastern France). We find generally weak soil moisture memory in mountainous areas (Alps, Massif central, Scandinavian mountains). Note that these large-scale patterns correspond with the spatial distribution of the fitted water holding capacities shown in Figure 3, pointing out the importance of the storing capacity for soil moisture memory. Also similar to the fitted water holding capacities, besides large-scale gradients there are also partly high small-scale variations (Germany, Norway). This highlights the importance of local soil and vegetation characteristics in comparison to the impact of the particular climate regime.

Interestingly, also for streamflow we find medium memory in many parts of Europe, especially in the Center and in the South-West, where soil moisture memory is also highest. Apart from these rather dominant large-scale variations we find also small-scale variations, as can be seen from the partly high memory differences between nearby catchments in central Europe, pointing out some importance of the role of local catchment characteristics also for

streamflow memory. Figure 5 shows moreover some memory in ET only for monthly data in some catchments in southern France. Possible reasons for this feature will be discussed in the following subsections.

4.3.2 Forcing memories and variabilities

As described in Section 2.1.1 streamflow depends on runoff (and therefore also on soil moisture and precipitation) and on the delay time scale τ (Equation (5)). Therefore streamflow memory may result from propagating soil moisture memory, but it is also induced by the delay time scale. ET depends on soil moisture and net radiation (Equation (2)) and hence its memory may stem from soil moisture memory or net radiation memory.

For daily data, net radiation memory and precipitation memory are negligible. Therefore ET memory results almost entirely from soil moisture memory, whereas streamflow memory is additionally impacted by the delay time scale. On the monthly time scale, however, we find small but no longer negligible memories for radiation and precipitation. Associated with that the forcing variabilities decrease towards longer time scales as day-to-day variations are averaged out. Note that the variability of radiation decreases more strongly than that of P_n^* as it already incorporates the joint impact of many daily precipitation sums.

4.3.3 Controls of memory propagation

To assess the connection between soil moisture memory versus streamflow and ET memory, a scatter plot of the streamflow and ET memories from all selected catchments as a function of the corresponding soil moisture memories is presented in Figure 6, where every point and every triangle represents one catchment. The left plot is based on daily data and shows 30-day-lag memories whereas the right plot is based on monthly data and shows 1-month-lag memories. In agreement with Figure 5, this analysis shows that ET memories are generally lower than streamflow memories. With the help of the dashed identity line we find that streamflow memory seems to be limited by the corresponding soil moisture memory, which suggests that streamflow memory to some extent originates from soil moisture memory. However, in two catchments the streamflow memory clearly exceeds the estimated soil moisture memory. This is because streamflow memory is not solely induced by soil moisture memory, but it may also be generated through the delay time scale τ, i.e. by (slow) transport of runoff water to the streambed and in the streambed towards the stream gauge station. The delay time scale that is among the longest in these 2 catchments. However, despite the impact of the delay time scale, the main control of streamflow memory is its

link with soil moisture memory as seen from the clear relationship in this plot.

Using color coding, Figure 6 also shows the respective soil moisture-streamflow and soil moisture-ET coupling strengths (see Section 2.5). Streamflow memories are found to be dependent on $\rho(S_n, w_n)$. Almost all catchments that show comparatively high streamflow memories, also show comparatively high $\rho(S_n, w_n)$ together with also relatively high soil moisture memories. This supports the above-described propagation of soil moisture memory. For the ET memory the link to $\rho(E_n, w_n)$ is less clear, nonetheless most of the catchments with comparatively high ET memory also display a higher $\rho(E_n, w_n)$. In most catchments $\rho(E_n, w_n)$ is weaker than $\rho(S_n, w_n)$, which explains why streamflow memory exceeds ET memory.

Whereas streamflow memories increase only slightly from daily to monthly time scales, the ET memories increase much stronger. This is because $\rho(E_n, w_n)$ increases stronger than $\rho(S_n, w_n)$ for most catchments, thanks to the strong reduction in radiation variability with increasing time scale (see Section 4.3.2). These findings highlight the importance of the time scale used in memory considerations. Although the forcing memories are no longer negligible on the monthly time scale (Section 4.3.2), Figure 6 illustrates that streamflow and ET memory are mostly controlled by soil moisture memory and the respective coupling strength, $\rho(E_n, w_n)$ or $\rho(S_n, w_n)$, as on the daily time scale.

When computing the memory of evaporative fraction $\frac{E_n}{R_n}$ instead of ET on the daily time scale (not shown) we find far stronger memory that is similar to soil moisture memory, underlining the strong weakening impact of daily net radiation variability on ET memory. Similarly, the memory of $\frac{Q_n}{P_n}$ is similar to soil moisture memory on the daily time scale (not shown), and therefore stronger than that of streamflow, which underlines the weakening impact of day-to-day precipitation variability.

Summing up, we have shown in this section that streamflow and ET memory depend on (i) soil moisture memory, which also acts to some extent as an upper limit, (ii) the strength of the coupling to soil moisture, and (iii) the memory of the forcing (predominantly on longer time scales). Furthermore streamflow memory may be generated by the delay time scale τ reflecting the conversion of runoff to streamflow. A schematic view of these dependencies is presented in Figure 7, with positive relationships denoted by red arrows and negative relationships shown with blue arrows. It also illustrates that the forcing memory not only supports the streamflow and ET memories but also the soil moisture memory itself (*Orth and Seneviratne* 2012). Moreover the scheme includes controls of $\rho(S_n, w_n)$ and $\rho(E_n, w_n)$, which are discussed in the following subsection together with a further discussion of Figure 7.

4.4 Soil moisture-streamflow and soil moisture-ET coupling

4.4.1 Geographical distribution

Figure 8 displays the geographical distribution of the two coupling strengths introduced in Section 2.5 and computed with daily and monthly averaged data, respectively. The geographical patterns appear to be independent of the applied averaging time scale. As seen previously for the streamflow and ET memories, the soil moisture-streamflow coupling strengths are similar for different time scales whereas the (absolute values of the) soil moisture-ET coupling strengths increase significantly in many catchments. This is also reflected in a clear increase of the standard deviation of all respective soil moisture-ET coupling strengths.

The soil moisture-streamflow coupling $\rho\left(S_n, w_n\right)$ is overall clearly stronger than the soil moisture-ET coupling $\rho\left(E_n, w_n\right)$. It is comparatively weak in coastal areas (Great Britain, Norway) and rather strong in flat, continental regions (Germany, France). However, in coastal areas around the Baltic sea (Denmark, Estonia, Finland) there is no reduction in $\rho\left(S_n, w_n\right)$. Overall, large-scale variations are dominant, although in some regions (e.g. Norway and Great Britain) partly great differences are found for nearby catchments.

For the soil moisture-ET coupling $\rho\left(E_n, w_n\right)$ small-scale variations are more prominent than large-scale variations, especially on the monthly time scale. In southern France the coupling is particularly strong due to the dry regime under which soil moisture is rather low and the ET function slope rather high (see Section 4.2). Negative $\rho\left(E_n, w_n\right)$ as seen at the monthly time scale for some catchments in central and northern Europe can be explained with very low slopes of the fitted ET ratio functions in these catchments; as a consequence ET depends almost entirely on net radiation which is usually negatively related with precipitation and hence soil moisture.

4.4.2 Controls

Having shown that streamflow and ET memory are originating from soil moisture memory and are furthermore controlled by the respective soil moisture-streamflow and soil moisture-ET coupling strengths, we analyze here the two coupling strengths themselves. Thereby we determine which climatic regime or catchment characteristics support or inhibit memory propagation. As shown in Figure 7, we investigate and identify two controls for the coupling strengths: (i) the slopes of the runoff (normalized by precipitation) and ET (normalized by net radiation)

functions (Equations (5) and (2); and shown exemplary for the Le Saulx catchment in Figure 4), (ii) the variance of the forcing, i.e. of cumulative weighted precipitation (P_n^*, Eq. (6)) and net radiation (R_n). We consider the forcing variances as they influence the translation of a soil moisture signal into streamflow and/or ET. For instance even if the respective slope is high, the respective coupling strength may be reduced by a high forcing variance.

Figure 9 shows the impact of both drivers described above on the two coupling strengths for daily and monthly averaged data. Every point (streamflow) and every triangle (ET) represents one catchment. The respective slopes of the fitted runoff and ET functions are plotted on the y-axes and the forcing variances can be read from the color coding of the symbols.

Focusing on ET first, we find increasing $\rho\left(E_n, w_n\right)$ with increasing mean slope of the ET function on both time scales. The radiation variances are very similar at all catchments. When comparing the variances from different time scales we find a clear reduction towards the longer, monthly time scale (see also Section 4.3.2). This is because day-to-day variations are averaged out, which also causes a stronger increase of $\rho\left(E_n, w_n\right)$ with increasing slope of the ET function.

Interestingly, $\rho\left(S_n, w_n\right)$ does not increase with increasing runoff function slope, but instead it decreases slightly on both considered time scales. Apart from the slope, $\rho\left(S_n, w_n\right)$ is also controlled by the variance of the atmospheric forcing (cumulative weighted precipitation P_n^*). Different precipitation variances cause a gradient in the coupling strengths of catchments with similar slopes. The rather strong role of the precipitation variance for $\rho\left(S_n, w_n\right)$ compared to the role of the radiation variance for the soil moisture-ET coupling is due to the much larger spread of the precipitation variances between all catchments, as shown in the color bars in Figure 9. Note, however, that the displayed variance of P_n^* is not strictly a forcing variance as P_n^* is determined in part by the delay time scale τ (see Equation (6)), which means consequently that also τ may impact $\rho\left(S_n, w_n\right)$.

The scheme in Figure 7 summarizes all the relationships investigated above. It also illustrates how $\rho\left(S_n, w_n\right)$ and $\rho\left(E_n, w_n\right)$ feed back on soil moisture memory. The stronger streamflow and ET respond to soil moisture, the more they tend to dampen initial soil moisture anomalies. For instance a dry anomaly causes a decrease in streamflow and ET, whereas a wet soil moisture anomaly would cause a strong increase, especially in streamflow (see Figure 4). The impact of the initial soil moisture anomaly for the subsequent soil moisture memory is discussed in Section 4.5. The variability of the forcings (precipitation and radiation) may weaken the streamflow and ET memory, but this effect only plays a role in case of low slopes of the runoff and ET functions, as seen especially for streamflow in Figure 9.

4.4.3 Differences between soil moisture-streamflow and soil moisture-ET coupling

As discussed in Section 4.3.3, streamflow memory exceeds ET memory in almost all catchments on the daily time scale and in most catchments on the monthly time scale. This is caused by the stronger coupling of streamflow to soil moisture ($\rho(S_n, w_n) > \rho(E_n, w_n)$) found in most catchments. The reason for this is that the runoff function slopes typically exceed the ET function slopes in the investigated catchments. Also the forcing variabilities play a role. As described in Section 4.3.3, they decrease with increasing time scale because day-to-day variations are averaged out, but the radiation variability decreases stronger, which explains why the ET memory increases more than the streamflow memory with increasing time scale.

The larger runoff function slopes and the consequently stronger impact of streamflow on soil moisture dynamics compared to the impact of ET on soil moisture dynamics are furthermore another reason for the considerable spread of the triangles in Figure 9. Catchments with similar ET function slopes may have very different runoff function slopes that impact soil moisture dynamics differently, thereby causing different $\rho(E_n, w_n)$. It should be noted that these results are likely dependent on the climatic region where the catchments are located (as the considered catchments are mostly located in central and northern Europe, i.e. in rather radiation-limited conditions).

4.5 Relating memory to persistence time scales

In Section 2.4 we introduced a methodology to compute time scales of persistence. Applying this methodology to the (modeled) streamflow and soil moisture data from the 100 selected catchments we derive maps of the mean persistences of dry and wet anomalies of medium and high strength in Figure 10. The geographical patterns of the persistences compare generally well to the mean memories derived from daily data as shown in Figure 5, suggesting consistency between the different approaches for memory computation. Note that partly strong small-scale variations of persistence are due to the heterogeneous nature of soil and vegetation characteristics. For soil moisture we find median persistences over the considered catchments ranging from 17 to 25 days depending on the considered anomaly. For streamflow the medians of the persistence time scales range between 5 and 7 days. Note that we do not investigate persistence in ET here as there is almost no memory on the daily time scale as shown previously in Figure 5. We find that it takes generally longer to recover to normal conditions from strong anomalies than from medium anomalies. In other words, the stronger an initial anomaly, the more pronounced is the following memory effect. While this is not unexpected, it has important implications for the forecasts of

443 extreme events. Also previous studies reported an enhanced soil moisture memory following hydrological extreme
444 conditions (*Koster et al.* 2010, *Orth and Seneviratne* 2012). This impact of the initial soil moisture anomaly on
445 the strength of the subsequent memory is also included in the schematic provided in Figure 7.

446 Comparing persistences of dry and wet anomalies we find that for soil moisture dry anomalies persist longer,
447 even if the difference to the persistence of wet anomalies is small in comparison to the absolute value of the
448 persistences. The reason for this result may be that the climate in most considered European catchments is
449 generally humid which means that dry anomalies can be very extreme whereas wet anomalies are rather limited (as
450 it cannot get much wetter). Unlike the soil moisture patterns, streamflow memory shows similar strength during
451 dry and wet anomalies. While the propagating soil moisture memory supports the streamflow memory especially
452 during dry anomalies, this result is due to the fact that $\rho\left(S_n, w_n\right)$ is stronger under wet conditions (see Section
453 4.2) which allows a better propagation of the soil moisture memory to streamflow (see Section 4.3.3). Note that
454 streamflow persistences for strong, dry anomalies could not be computed for all selected catchments as in some
455 catchments the respective threshold is only exceeded on very few days. This is because streamflow values rather
456 follow an exponential than a normal distribution.

457 Figure 11 displays a comparison of memories computed as lag correlation and as persistence time scales.
458 As above, we focus on soil moisture and streamflow, and we additionally investigate observed streamflow. The
459 reasonably high R^2 values of the linear fits indicate consistency between the two approaches, only persistence time
460 scales computed for dry (modeled and observed) streamflow anomalies correspond less well to the respective lag
461 correlations due to the exponential distribution of the streamflow values discussed above. Figure 11 also shows
462 that dry soil moisture anomalies persist longer than respective wet anomalies whereas for streamflow we find
463 the opposite for the weaker anomalies of 1.33 standard deviation considered here. The results for modeled and
464 observed streamflow are similar, indicating a good representation of streamflow memory/persistence in the simple
465 water balance model (which is not surprising, however, as the model is calibrated with observed streamflow).
466 The logarithmic scale of the persistence time scales indicates interestingly that persistence time scales increase
467 exponentially for a linear increase in estimated lag correlation. This underlines the red noise character of soil
468 moisture, which was already reported by *Delworth and Manabe* (1988). Note that the findings of this figure are
469 robust, even if we consider persistence time scales related to other anomaly thresholds or lag correlations of other
470 time lags.

5 Conclusions

Using data from 100 catchments located across Europe we have shown that a simple water balance model is able to simulate realistic streamflow as well as realistic streamflow memory characteristics compared to observations, thereby expanding the validation earlier performed by *Orth et al.* (2013).

Further, this study investigated the connection between soil moisture memory and both streamflow and ET memory. We showed that soil moisture memory to some extent serves as an upper bound for streamflow and ET memory. Furthermore we defined measures of the coupling between soil moisture and streamflow as well as between soil moisture and ET and found that the strengths of these couplings also determine the memory strength of streamflow and ET, respectively. These findings explain why one can infer that the memory *propagates* from soil moisture to streamflow and ET as illustrated in Figure 7. As streamflow and ET are moreover driven by the meteorological forcing, also the (small) memories of cumulative weighted precipitation and net radiation (only on the monthly time scale) play a (minor) role for the strength of their respective memories.

Comparing the results for daily and monthly time scales we generally find higher memory for monthly averaged data and for all three quantities. This is due to the reduced impact of the day-to-day variations of the meteorological forcing.

Figure 7 also displays the special role of the coupling strengths between soil moisture and streamflow as well as between soil moisture and ET. We showed that the soil moisture-ET coupling is mostly controlled by the slope of the fitted (normalized) ET function whereas the soil moisture-streamflow coupling is strongly related to the variance of the weighted cumulative precipitation. In most catchments, the ET function slope is smaller than the runoff function slope, which is the main reason for the generally weaker coupling between soil moisture and ET and the consequently lower ET memory as compared to streamflow memory.

In the last part of this study we introduced an alternative approach for computing memory to study its dependency on different hydrological conditions. Instead of using a lag correlation we calculated the mean time required to recover from anomalous conditions above a certain threshold to normal conditions. Applying the new methodology we found increased memory under more extreme conditions, as illustrated in Figure 7 by the positive impact of the initial soil moisture anomaly on subsequent soil moisture memory. We further point out that soil moisture memory is strongest for dry anomalies whereas streamflow memory is stronger during wet anomalies (in the investigated catchments). These results have important implications for sub-seasonal forecasts of dry and wet soil moisture and streamflow anomalies, including drought and flood events. As the resulting

persistence time scales are expressed in days, this measure of memory it is more easily interpretable, which is of particular relevance for applications and practitioners. We show consistency between the two approaches, which is furthermore underlined by the consistency of the derived geographical soil moisture and streamflow memory patterns. We also find that the persistence time scales are exponentially related to the respective lag correlations, pointing out a special importance of high lag correlations identified for soil moisture.

Acknowledgments

We acknowledge the Swiss National Foundation for financial support through the NRP61 DROUGHT-CH project. Furthermore we acknowledge the European water archive and the EU-FP6 project WATCH (http://www.eu-watch.org [checked on 28 September 2012]) for sharing streamflow data. We acknowledge the E-OBS dataset from the EU-FP6 project ENSEMBLES (http://ensembles-eu.metoffice.com [checked on 28 September 2012]) and the data providers in the ECA&D project (http://www.ecad.eu [checked on 28 September 2012]) for precipitation data as well as the NASA/GEWEX SRB project (http://eosweb.larc.nasa.gov/PRODOCS/srb/table_srb.html [checked on 28 September 2012]) for sharing radiation data with us. We thank two anonymous reviewers as well as Christof Appenzeller and Randy Koster for helpful comments on the manuscript

Appendix A: Overview of catchments

Catchment (river)	Country	Gauging station	Size (km^2)	Mean altitude (m above sea level)	Mean daily stream-flow (mm)	Catchment centroid
Antiesen	Austria	Haging	165	512	1.35	48.3°N 13.4°E
Braunaubach	Austria	Hoheneich	292	580	0.60	48.8°N 15.0°E
Griesler Ache	Austria	St. Lorenz	122	732	2.99	47.8°N 13.3°E
Große Rodl	Austria	Rottenegg	226	703	1.19	48.3°N 14.1°E
Große Tulln	Austria	Siegersdorf	202	348	0.51	48.3°N 15.9°E
Leogangbach	Austria	Uttenhofen	112		2.14	47.4°N 12.8°E
Traun	Austria	Obertraun	334	1078	5.39	47.6°N 13.7°E
Otava	Czech Republic	Rejtejn	334	1025	2.22	49.1°N 13.5°E
Svratka	Czech Republic	Borovnice	128		0.97	49.7°N 16.2°E
Teplá Vltava	Czech Republic	Lenora	176	1018	1.47	48.9°N 13.8°E
Volynka	Czech Republic	Nemetice	383	728	0.63	49.2°N 13.9°E
Vantaa	Finland	Oulunkylä	1680	78	0.90	60.2°N 25.0°E
L' Aisne	France	Mouron	2239	208	0.95	49.3°N 4.8°E
L' Ance Du Nord	France	St-Julien-D'ance (Laprat)	354	995	1.01	45.3°N 3.9°E
Le Bes	France	St-Juery	283	1200	2.10	44.8°N 3.1°E
La Colagne	France	St-Amans (Ganivet)	89	1286	1.30	44.7°N 3.4°E
Le Doubs	France	Goumois	1060	992	2.36	47.3°N 7.0°E
La Drome	France	Luc-En-Diois	194	1014	1.02	44.6°N 5.4°E
La Loire	France	Bas-En-Basset	3234	968	0.90	45.3°N 4.1°E
La Moselle	France	St-Nabord (Noir Gueux)	633	720	3.35	48.1°N 6.6°E
Le Saulx	France	Vitry-En-Perthois	2109	264	1.12	48.7°N 4.6°E
La Seine	France	Bar-Sur-Seine	2344	320	0.94	48.1°N 4.4°E
La Sioule	France	St-Priest-Des-Champs (Fades-Besserve)	1305	781	1.08	46.0°N 2.8°E
La Tardes	France	Evaux-Les-Bains	854	507	0.84	46.2°N 2.4°E
La Truyere	France	Malzieu-Ville (Le Soulier)	582	1122	1.13	44.8°N 3.3°E
La Truyere	France	Neuveglise (Grandval)	1803	1069	1.17	44.9°N 3.1°E

Catchment (river)	Country	Gauging station	Size (km^2)	Mean altitude (m above sea level)	Mean daily stream-flow (mm)	Catchment centroid
Aitrach	Germany	Lauben	308	732	1.52	47.9°N 10.0°E
Apfelstädt	Germany	Ingersleben	371	449	0.60	50.9°N 11.0°E
Attel	Germany	Anger	244	523	1.39	48.0°N 12.2°E
Brugga	Germany	Oberried-Ibrech	40	989	3.41	47.9°N 8.0°E
Dhron	Germany	Papiermühle	170	489	0.95	49.8°N 6.9°E
Elsava	Germany	Rück	145	356	0.72	49.8°N 9.2°E
Engnitz	Germany	Hüttengrund	46	654	2.08	50.4°N 11.2°E
Gaissa	Germany	Hoerrmannsberg	212	457	1.30	48.7°N 13.4°E
Grosse Ohe	Germany	Schönberg	82	811	2.13	48.8°N 13.4°E
Grosser Regen	Germany	Zwiesel	177	886	2.52	49.0°N 13.2°E
Helme	Germany	Sundhausen	201	255	0.76	51.5°N 10.8°E
Kinzig	Germany	Schwaibach	964	600	2.16	48.4°N 8.0°E
Kollbach	Germany	Deggendorf	36		1.73	48.8°N 13.1°E
Lahn	Germany	Biedenkopf	309	477	1.60	50.9°N 8.5°E
Lohr	Germany	Partenstein	217	400	1.20	50.0°N 9.5°E
Mindel	Germany	Offingen	951	595	1.14	48.5°N 10.4°E
Mitternacher Oh	Germany	Eberhardsreuth	114	663	1.55	48.8°N 13.4°E
Osterbach	Germany	Röhrnbach	121	645	1.88	49.0°N 13.2°E
Reschwasser	Germany	Unterkashof	61	967	2.69	48.9°N 13.5°E
Rodach	Germany	Streitmühle bei Due	55	633	1.55	50.4°N 11.5°E
Rottach	Germany	Rottach	31	1159	2.88	47.7°N 11.8°E
Saalach	Germany	Unterjettenberg Rech	760	1211	3.34	47.7°N 12.8°E
Schwarzwasser	Germany	Aue1	362	745	1.51	50.6°N 12.7°E
Sinn	Germany	Mittelsinn	461	456	1.19	50.2°N 9.6°E
Steinacher Ache	Germany	Fallmuehle	22	1355	3.73	47.6°N 10.5°E
Stoisser Ache	Germany	Piding	50	738	2.08	47.8°N 12.9°E
Tiroler Achen	Germany	Staudach	944	1139	3.21	47.8°N 12.5°E
Traun	Germany	Stein Bei Altenmarkt	378	850	2.85	48.0°N 12.6°E
Uessbach	Germany	Peltzerhaus	176	410	0.84	50.1°N 7.1°E
Ulster	Germany	Guenthers	182	598	1.38	50.7°N 10.0°E
Untere Steinach	Germany	Oberhammer	67	576	1.44	50.2°N 11.5°E
Vils	Germany	Pfronten Ried	110	1369	3.78	47.6°N 10.6°E
Weisser Regen	Germany	Koetzing	226	692	1.72	49.3°N 13.0°E
Wertach	Germany	Biessenhofen	442	882	2.44	47.8°N 10.7°E
Weschnitz	Germany	Lorsch	383	214	0.71	49.7°N 8.6°E
Wipper	Germany	Hachelbich	524	324	0.63	51.3°N 11.0°E

Catchment (river)	Country	Gauging station	Size (km^2)	Mean altitude (m above sea level)	Mean daily stream-flow (mm)	Catchment centroid
Årgårdselv	Norway	Øyungen	230	316	4.51	64.2°N 11.1°E
Engesetelev	Norway	Engsetvatn ndf	41	206	4.92	62.5°N 6.6°E
Etna	Norway	Etna	565	925	1.44	61.0°N 9.6°E
Etneelv	Norway	Stordalsvatn	140	611	9.09	59.7°N 6.0°E
Flisa	Norway	Knappom	1655	414	1.38	60.6°N 12.0°E
Forra	Norway	Høggås bru	458	525	3.77	63.5°N 11.4°E
Fusta	Norway	Fustvatn	520	472	5.58	65.9°N 13.3°E
Glomma	Norway	Atnasjø	468	1140	1.85	61.9°N 10.2°E
Guddalselva	Norway	Nautsundvatn	214	436	7.17	61.3°N 5.4°E
Jondalselv	Norway	Jondal	150	569	1.73	59.7°N 9.6°E
Kløvtveitelv	Norway	Kløvtveitvatn	5	466	11.06	61.0°N 5.3°E
Lygna	Norway	Tingvatn	265	564	5.80	58.4°N 7.2°E
Moelv	Norway	Salsvatn	435	285	5.18	64.7°N 11.5°E
Nordelva	Norway	Krinsvatn	210	435	5.42	63.8°N 10.2°E
Ogna	Norway	Helleland	75	336	6.79	58.5°N 6.2°E
Øren	Norway	Øren	151	264	4.05	62.8°N 7.7°E
Oselv	Norway	Røykenes	55	328	8.63	60.3°N 5.4°E
Strandå	Norway	Strandå	27	212	5.89	67.5°N 14.9°E
Tovdalselv	Norway	Austenå	310	752	3.01	58.8°N 8.1°E
No name	Norway	Karpelv	129	194	1.72	69.7°N 30.4°E
Biely Vah	Slovakia	Vychodna	106	1055	1.26	49.0°N 19.9°E
Kysuca	Slovakia	Cadca	492	647	1.46	49.4°N 19.0°E
Poprad	Slovakia	Poprad-Matejovce	311	1001	1.13	49.1°N 20.3°E
Rajcianka	Slovakia	Poluvsie	243	706	1.18	49.1°N 18.7°E
Dalelven	Sweden	Ersbo	654	728	3.34	61.3°N 13.0°E
Moelven	Sweden	Anundsjön	1457	283	1.10	63.4°N 18.3°E
Kleine Emme	Switzerland	Littau	78		2.00	47.5°N 8.9°E
Murg	Switzerland	Waengi	477	662	2.79	47.1°N 8.3°E
Allan Water	United Kingdom	Kinbuck	172	245	3.07	56.2°N 3.9°W
Coln	United Kingdom	Bibury	107	181	1.12	51.8°N 1.8°W
Cree	United Kingdom	Newton Stewart	368	243	3.77	55.0°N 4.5°W
Dart	United Kingdom	Austins Bridge	249	327	3.91	50.5°N 3.8°W
Dee	United Kingdom	Woodend	1394	512	2.46	57.1°N 2.6°W
Kinnel Water	United Kingdom	Redhall	78	245	3.45	55.2°N 3.4°W
Nith	United Kingdom	Friars Carse	812	293	3.28	55.1°N 3.7°W
Thet	United Kingdom	Melford Bridge	315	40	0.53	52.4°N 0.8°E
Tweed	United Kingdom	Boleside	1559	361	2.31	55.6°N 2.8°W
Weaver	United Kingdom	Audlem	207	89	0.76	53.0°N 2.5°W

References

Bisselink, B., and A. J. Dolman (2009), Recycling of moisture in Europe: contribution of evaporation to variability in very wet and dry years, *Hydrol. Earth Syst. Sci.*, *13*, 1685–1697.

Botter, G., A. Porporato, I. Rodriguez-Iturbe, and A. Rinaldo (2007), Basin-scale soil moisture dynamics and the probabilistic characterization of carrier hydrologic flows: Slow, leaching-prone components of the hydrologic response, *Water Resources Research*, *43*, W02,417.

Delworth, T. L., and S. Manabe (1988), The influence of potential evaporation on the variabilities of simulated soil wetness and climate, *J. Climate*, *1*, 523–547.

Eagleson, P. S. (1978), Climate, soil and vegetation. The expected value of annual evapotranspiration, *Water Resources Research*, *14*, 731–739.

Entin, J. K., A. Robock, K. Y. Vinnikov, S. E. Hollinger, S. Liu, and A. Namkhai (2000), Temporal and spatial scales of observed soil moisture variations in the extratropics, *J. Geophys. Res.*, *105*, 11,865–11,877.

Gudmundsson, L., L. M. Tallaksen, K. Stahl, and A. K. Fleig (2011), Low-frequency variability of European runoff, *Hydrol. Earth Syst. Sci.*, *15*, 2853–2869.

Kirchner, J. (2009), Catchments as simple dynamical systems: Catchment characterization, rainfall-runoff modeling, and doing hydrology backward, *Water Resources Research*, *45*, W02,429.

Koster, R. D., and S. Mahanama (2012), Land Surface Controls on Hydroclimatic Means and Variability, *J. Hydrometeorol.*, *13*, 1604–1620.

Koster, R. D., and P. C. D. Milly (1997), The interplay between transpiration and runoff formulations in land surface schemes used with atmospheric models, *J. Climate*, *10*, 1578–1591.

Koster, R. D., and M. J. Suarez (2001), Soil moisture memory in climate models, *J. Hydrometeorol.*, *2*, 558–570.

Koster, R. D., et al. (2004), Regions of strong coupling between soil moisture and precipitation, *Science*, *305*, 1138–1140.

544 Koster, R. D., et al. (2010), Contribution of land surface initialization to subseasonal forecast skill: First results
545 from a multi-model experiment, *Geophys. Res. Lett.*, *37, L02402*.

546 Labat, D. (2008), Wavelet analysis of the annual discharge records of the world's largest rivers, *Advances in Water*
547 *Resources*, *31 (1)*, 109–117.

548 Lins, H. F. (1997), Regional streamflow regimes and hydroclimatology of the United States, *Water Resources*
549 *Research*, *33*, 1655–1667.

550 Mueller, B., and S. I. Seneviratne (2012), Hot days induced by precipitation deficits at the global scale, *Proc.*
551 *Natl. Acad. Sci.*, *109 (31)*, 12,398–12,403.

552 Orth, R., and S. I. Seneviratne (2012), Analysis of soil moisture memory from observations in Europe, *J. Geophys.*
553 *Res.*, *117*, D15,115, doi:10.1029/2011JD017366.

554 Orth, R., R. D. Koster, and S. I. Seneviratne (2013), Inferring soil moisture memory from runoff observations, *J.*
555 *Hydrometeorol., accepted with minor revisions*.

556 Robock, A., K. Y. Vinnikov, G. Srinivasan, J. K. Entin, S. E. Hollinger, N. A. Speranskaya, S. Liu, and A. Namkhai
557 (2000), The global soil moisture data bank, *Bull. Amer. Meteorol. Soc.*, *81*, 1281–1299.

558 Rodriguez-Iturbe, I., and J. B. Valdes (1979), The geomorphologic structure of hydrologic response, *Water Re-*
559 *sources Research*, *15*, 1409–1420.

560 Schlosser, C. A., and P. C. D. Milly (2002), A model-based investigation of soil moisture predictability and
561 associated climate predictability, *J. Hydrometeorol.*, *3*, 483–501.

562 Seneviratne, S. I., and R. D. Koster (2012), A revised framework for analyzing soil moisture memory in climate
563 data: Derivation and interpretation, *J. Hydrometeorol.*, *13*, 404–412.

564 Seneviratne, S. I., T. Corti, E. L. Davin, M. Hirschi, E. B. Jaeger, I. Lehner, B. Orlowsky, and A. J. Teuling
565 (2010), Investigating soil moisture-climate interactions in a changing climate: A review, *Earth-Science Reviews*,
566 *99*, 125–161.

567 Seneviratne, S. I., et al. (2006), Soil moisture memory in AGCM simulations: Analysis of Global Land-Atmosphere
568 Coupling Experiment (GLACE) data, *J. Hydrometeorol.*, *7*, 1090–1112.

569 Stahl, K., H. Hisdal, J. Hannaford, L. M. Tallaksen, H. A. J. van Lanen, E. Sauquet, S. Demuth, M. Fendekova,
570 and J. Jódar (2010), Streamflow trends in Europe: evidence from a dataset of near-natural catchments, *Hydrol.*
571 *Earth Syst. Sci.*, *14*, 2367–2382.

572 Teuling, A. J., et al. (2009), A regional perspective on trends in continental evaporation, *Geophys. Res. Lett.*, *36,*
573 *L02404*.

574 Vinnikov, K. Y., and I. B. Yeserkepova (1990), Soil moisture: Empirical data and model results, *J. Climate*, *4*,
575 66–79.

576 Wu, W., and R. E. Dickinson (2004), Time scales of layered soil moisture memory in the context of land-atmosphere
577 interaction, *J. Climate*, *17*, 2752–2764.

Table 1: Overview of model parameter accuracies, boundaries and the range of their respective estimates.

Parameter	Accuracy	Lower limit	Upper limit	Minimum value found	Maximum value found
water holding capacity c_s (mm)	30	20	2000	50	890
inverse streamflow recession timescale $\frac{1}{\tau}$ (1/days)	0.02	0.02	-	0.04	0.78
runoff exponent α	0.2	0	15	0.2	15
ET exponent γ	0.03	0	-	0.03	3.87
max ET ratio β_0	0.03	0.03	0.99	0.24	0.99

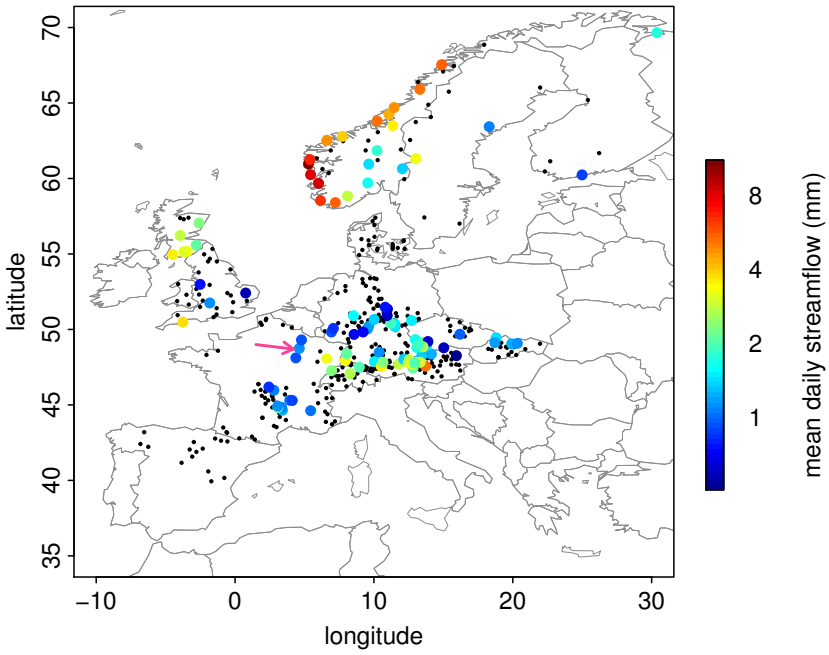

Figure 1: The colored large dots indicate the locations of the selected 100 catchments. The color coding indicates the mean daily streamflow between May and September. The smaller black dots indicate the locations of the remaining catchments of the *Stahl et al.* (2010) dataset, as considered for the validation of streamflow (memory) in Section 4.1. The arrow points to the Le Saulx catchment later considered in Section 4.2.

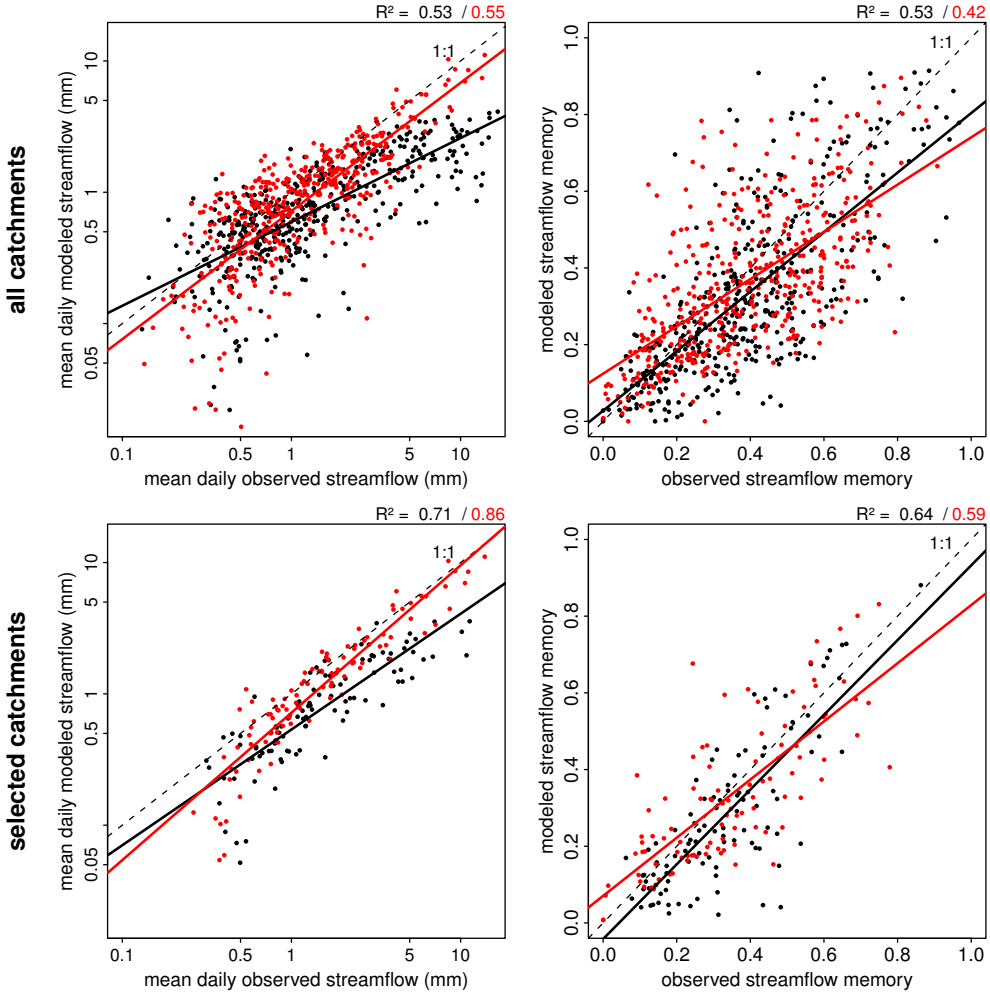

Figure 2: The left plots show modeled versus observed mean daily streamflows for June (in black) and October (in red). Note the logarithmic scale of both axes. The thick straight lines are fitted with least-squared regression, R^2 values shown on top are a result of this. The right plots show the same, only for mean monthly streamflow memory $\rho\left(S_n, S_{n+15\,days}\right)$. The upper row shows results for all 441 catchments, the lower row only contains the selected catchments.

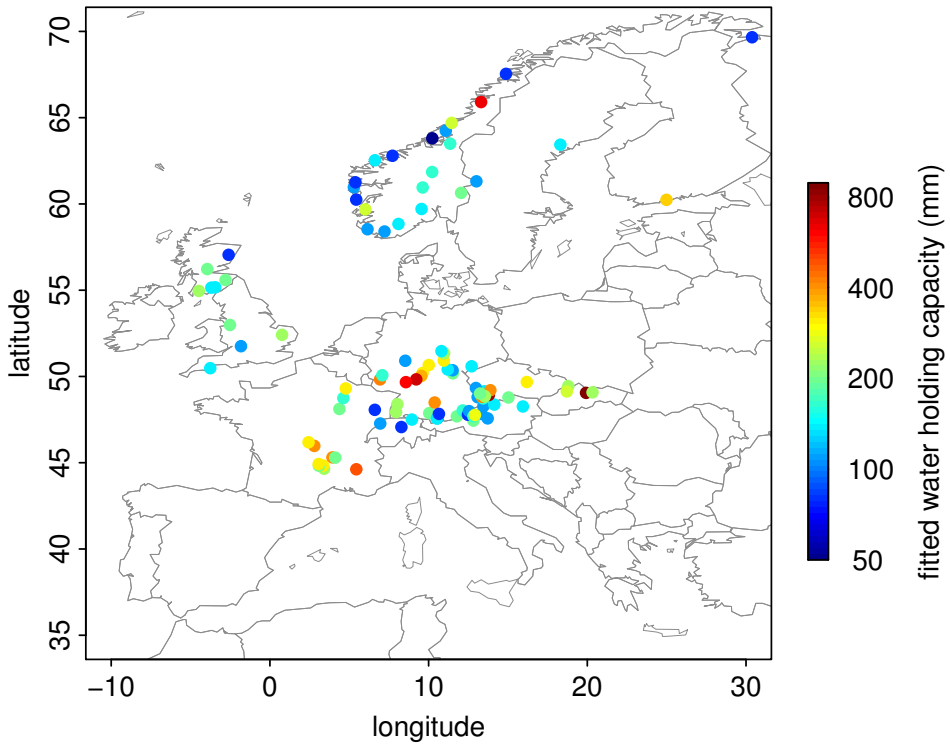

Figure 3: Fitted water holding capacites for the selected catchments. Note the logarithmic scale of the color-coding.

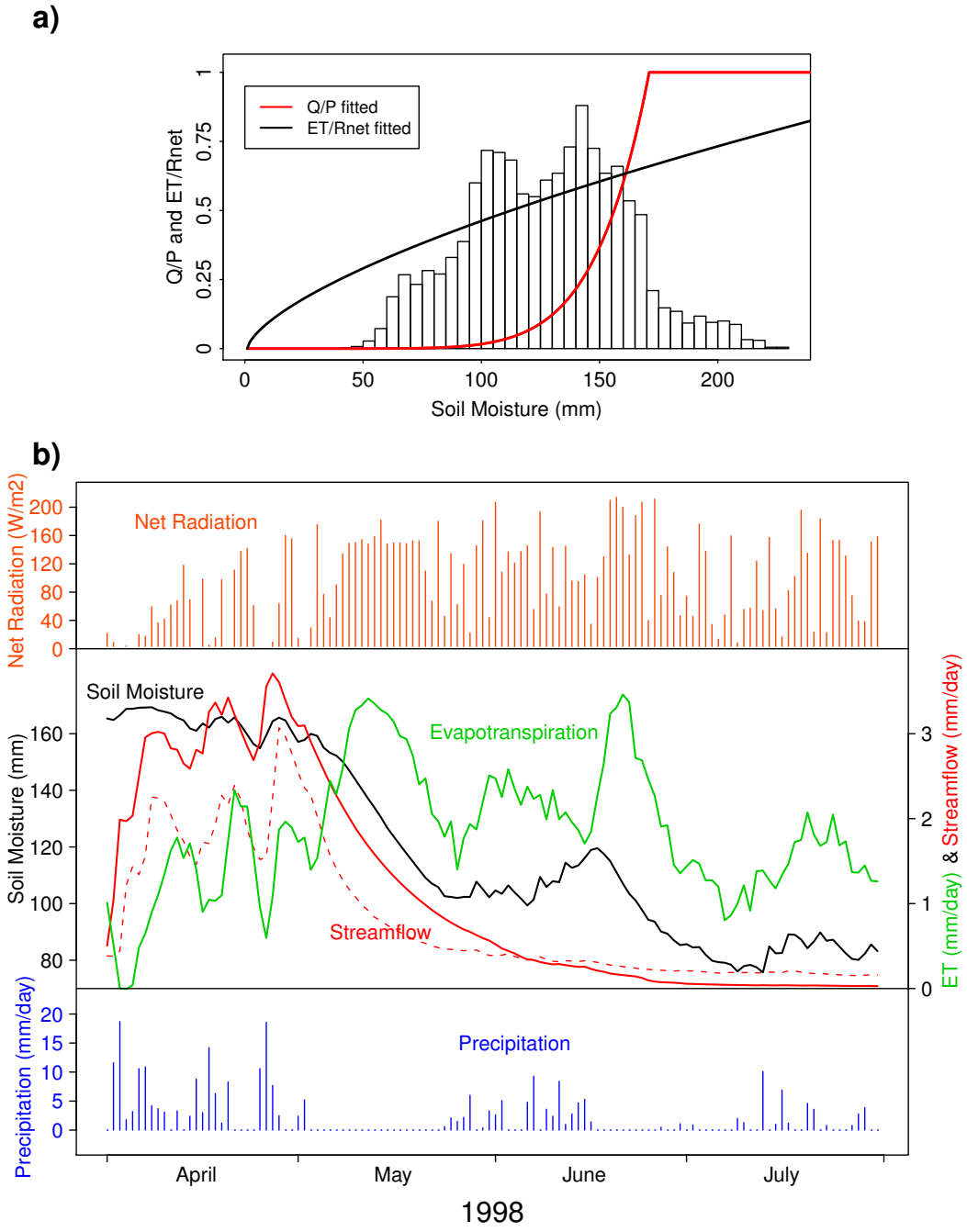

Figure 4: a) Fitted normalized streamflow (Equation (5)) and ET (Equation (2)) functions for the Le Saulx catchment in eastern France (indicated by an arrow in Figure 1). The background histogram shows the relative abundance of soil moisture contents between April and October.
b) Time series of forcing (net radiation at the top, precipitation at the bottom) and according output of the simple model (soil moisture, streamflow and ET in between the forcings) from the Le Saulx catchment during a pronounced dry-out period from April until July 1998. The dashed red line indicates the evolution of the observed streamflow. The fitted water holding capacity for this catchment is 170 mm, such that the normalized streamflow function reaches 1 at this soil moisture content. Note that the ET time series has been smoothed to facilitate the readability of the graph such that each value represents the average of the current day, the three preceding days and the three following days.

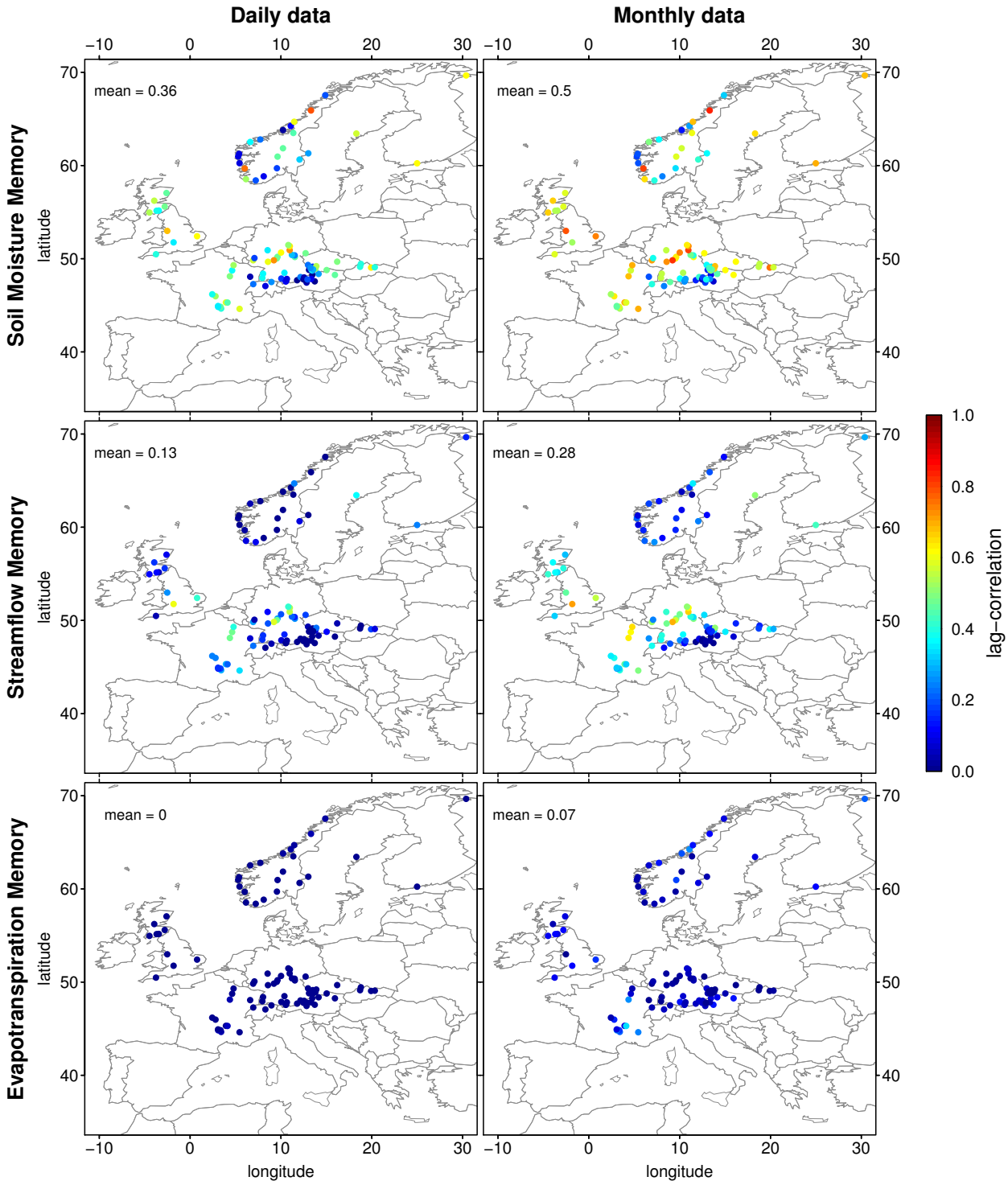

Figure 5: Geographical distribution of mean May-September memories of soil moisture ($\rho(w_n, w_{n+lag})$, upper row), streamflow ($\rho(S_n, S_{n+lag})$, center row) and ET ($\rho(E_n, E_{n+lag})$, lower row) for daily and monthly averaged data (all memories computed for a lag of 30 days (daily data) or 1 month (monthly data)) computed as described in Section 2.3.

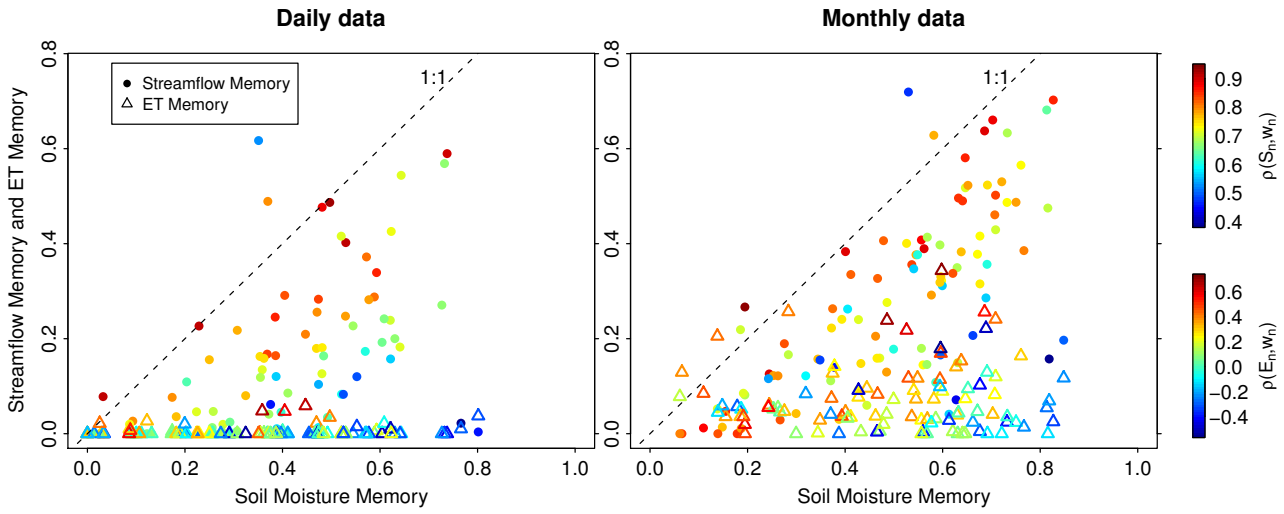

Figure 6: Streamflow (dots) and ET (triangles) memories $\rho\left(S_n, S_{n+lag}\right)$ and $\rho\left(E_n, E_{n+lag}\right)$, respectively, of all selected catchments plotted versus the corresponding soil moisture memories $\rho\left(w_n, w_{n+lag}\right)$ for daily and monthly averaged data (all memories computed for a lag of 30 days (daily data) or 1 month (monthly data)). The color coding denotes the strength of the soil moisture-streamflow coupling $\rho\left(S_n, w_n\right)$ and the soil moisture-ET coupling $\rho\left(E_n, w_n\right)$, respectively (see Section 2.5).

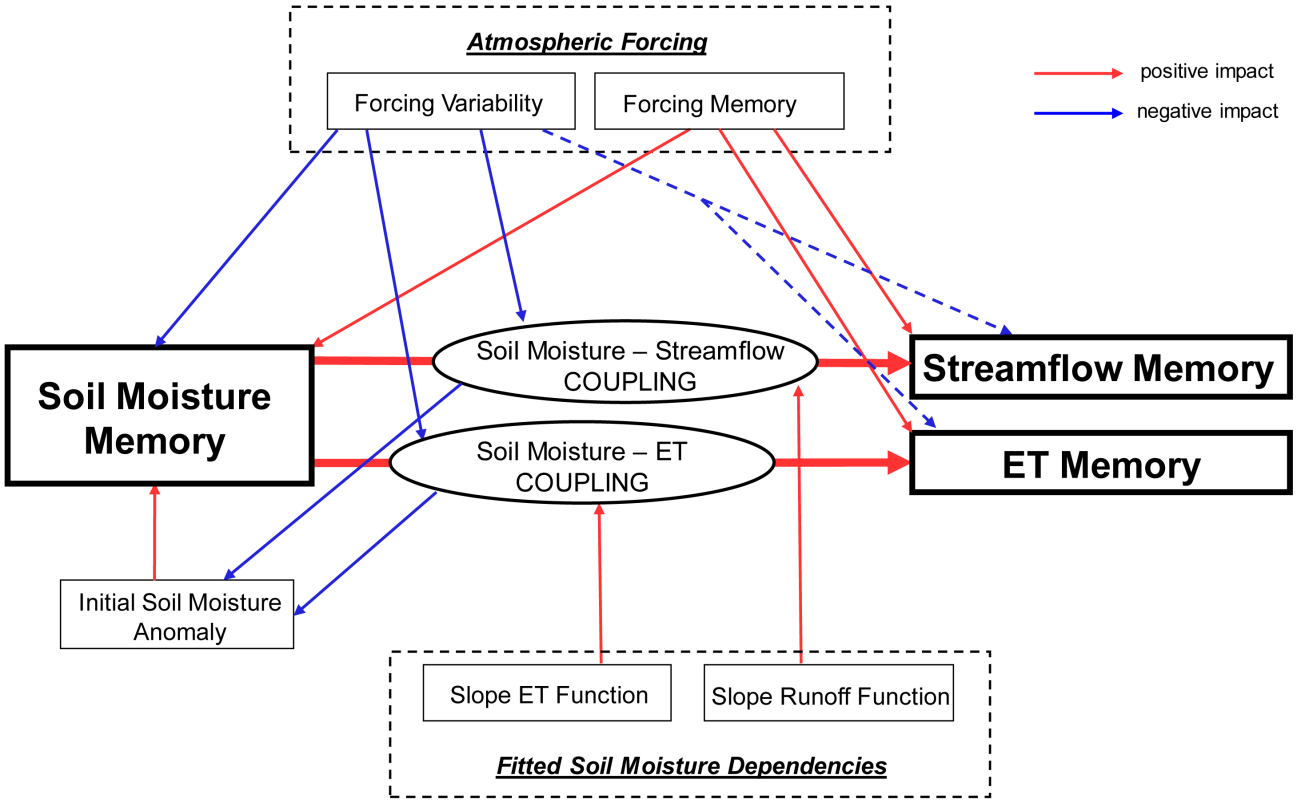

Figure 7: Schematic view of propagation of soil moisture memory to streamflow memory and ET memory. Red arrows denote positive impacts, blue arrows show negative impacts. Only dependencies investigated in this study are shown.

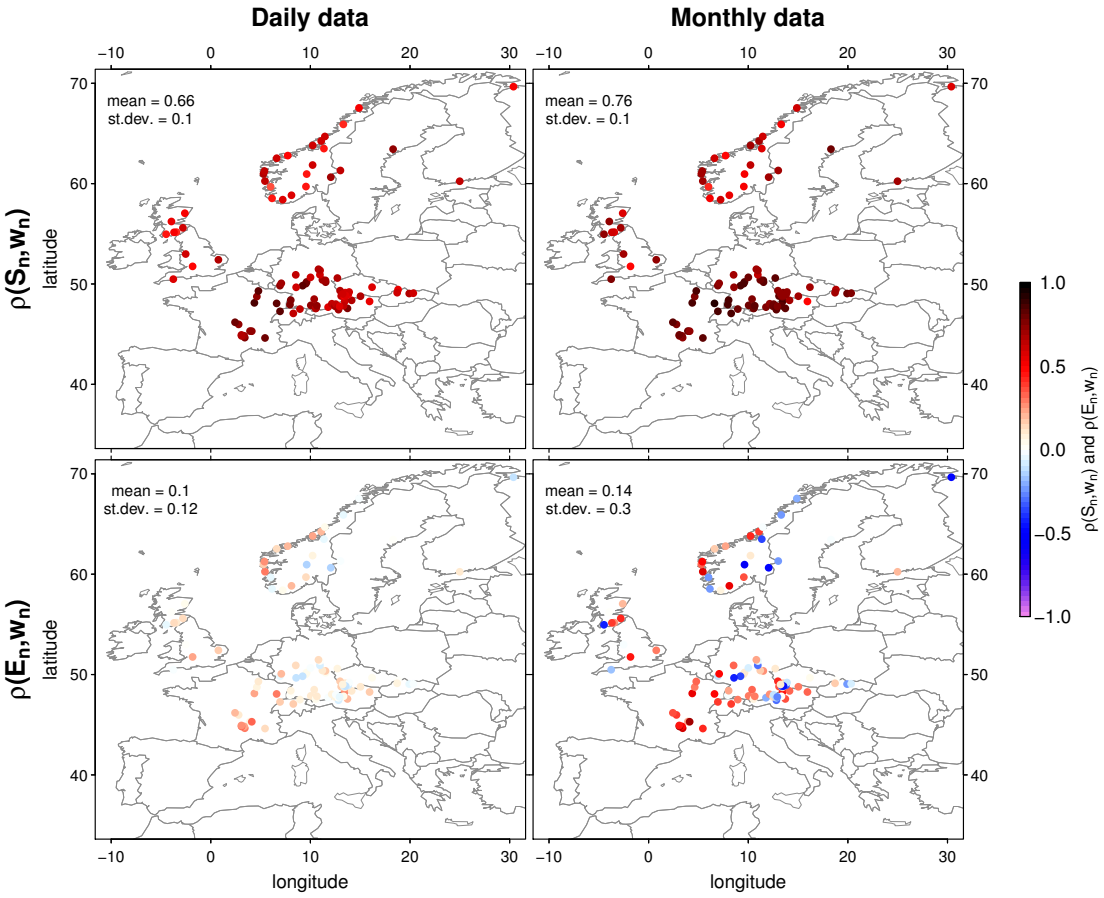

Figure 8: Geographical distribution of mean May-September soil moisture-streamflow (upper row) and soil moisture-ET (lower row) coupling strengths $\rho(S_n, w_n)$ and $\rho(E_n, w_n)$, respectively, for daily and monthly averaged data. Respective strengths are shown through the color coding. In the upper left corner of each plot the mean and standard deviation over the selected catchments are displayed.

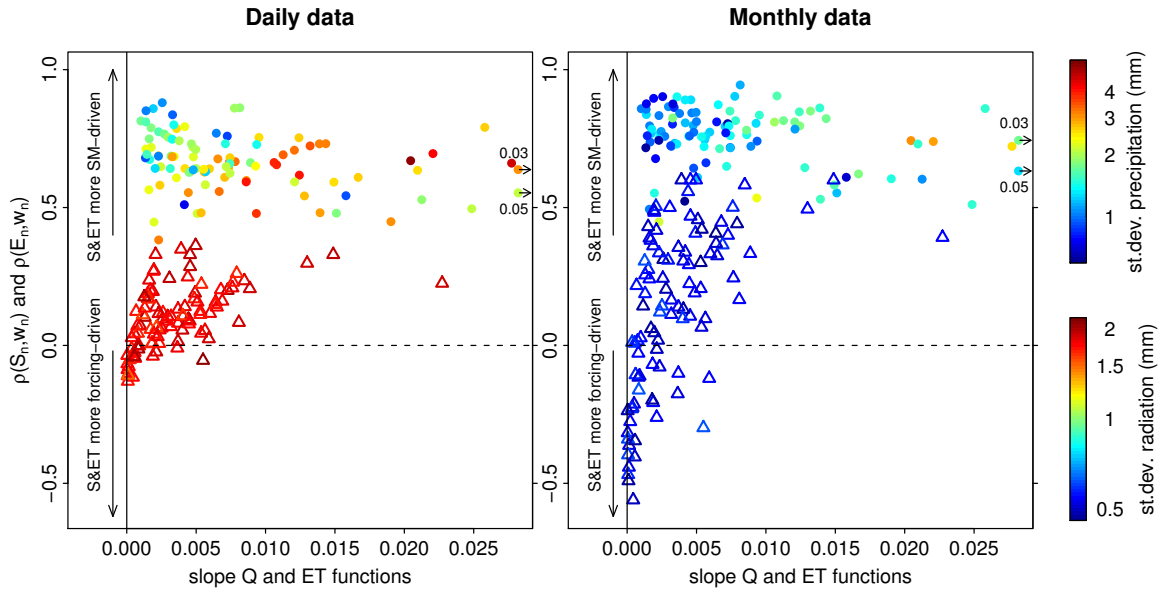

Figure 9: Soil moisture-streamflow (dots) and soil moisture-ET (triangles) coupling strengths, $\rho(S_n, w_n)$ and $\rho(E_n, w_n)$, respectively, plotted against the respective runoff and ET function slope (computed as described in Section 4.4.2) for daily and monthly averaged data. The color coding denotes the variance of the weighted precipitation sum precipitation (P_n^*) and of radiation, respectively. All involved quantities computed as means from May-September. Points that do not fit with the range of the x- and/or y-axis are also included together with an arrow pointing in the direction of their actual location and the true value displayed next to it.

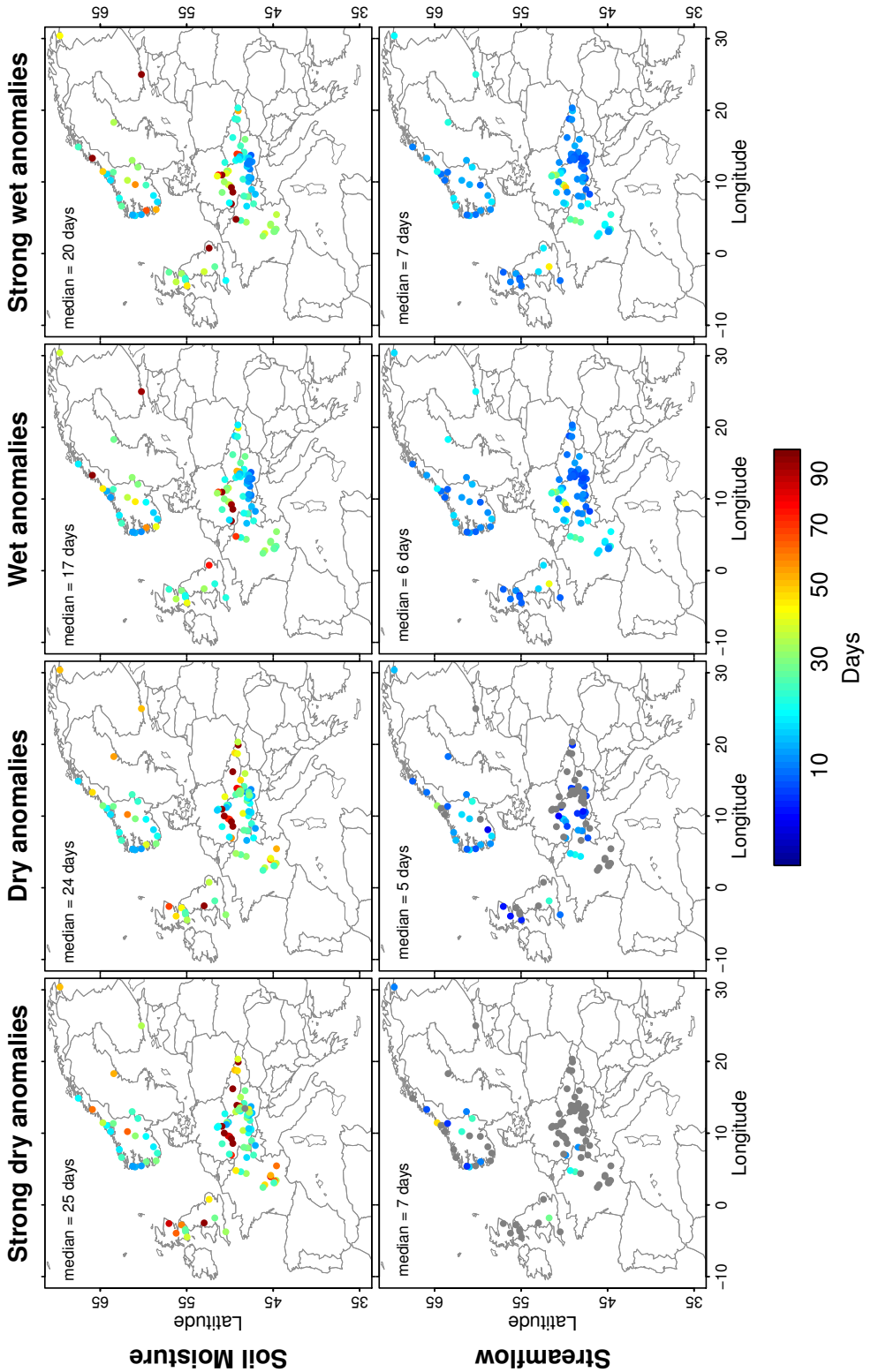

Figure 10: Overview of mean durations to recover from (very) dry/wet conditions (1.33 and 1.66 standard deviations away from the respective daily mean of the respective quantity) to normal conditions ($\pm$ 1 standard deviation around the mean) for (modeled) soil moisture and streamflow. The results are based on daily data. In the upper left corner of each plot the median over all selected catchments is displayed. Gray color indicates that no persistence can be computed because the applied threshold is almost never reached.

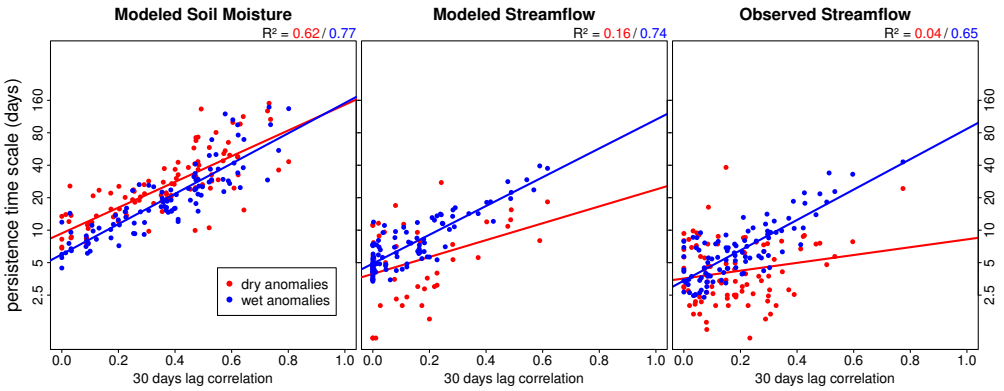

Figure 11: Comparison of memory estimates computed as lag correlation and as persistence time scale (based on anomalies of 1.33 standard deviations from the mean) for modeled soil moisture and streamflow (left and middle) and observed streamflow (right). Red points refer to persistence time scales estimated from dry anomalies whereas blue points are derived from wet anomalies. The red and blue lines denote the respective linear least-squares fit. Note the logarithmic scale of the persistence time scale.